

## Article

# Impact of Silica-Modification and Oxidation on the Crystal Structure of Magnetite Nanoparticles

Artur Dzeranov <sup>1,2</sup>, Lyubov Bondarenko <sup>1,\*</sup>, Denis Pankratov <sup>3</sup>, Gulzhian Dzhardimalieva <sup>1,4</sup>, Sharipa Jorobekova <sup>5</sup>, Daniel Saman <sup>1</sup> and Kamila Kydralieva <sup>1</sup>

<sup>1</sup> Moscow Aviation Institute (National Research University), Moscow 125993, Russia

<sup>2</sup> Sklifosovsky Institute for Emergency Medicine, Moscow 129090, Russia

<sup>3</sup> Department of Chemistry, Lomonosov Moscow State University, Moscow 119991, Russia

<sup>4</sup> Federal Research Center of Problems of Chemical Physics and Medicinal Chemistry, Russian Academy of Sciences, Chernogolovka 142432, Moscow Region, Russia

<sup>5</sup> Institute of Chemistry and Phytotechnologies, National Academy of Sciences, Bishkek 720071, Kyrgyzstan

\* Correspondence: l.s.bondarenko92@gmail.com

**Abstract:** At present, the widespread use of iron oxide nanoparticles, including for commercial purposes, requires strict preservation of their phase composition during their application. The choice of nanoparticle modifier and modification conditions is decisive due to their high sensitivity to oxygen in the case of using real conditions (O<sub>2</sub>, pH change, etc.). In this work, we studied the change in the phase composition of magnetite nanoparticles after modification with 3-aminopropyltriethoxysilane (APTES) and oxidation with nitric acid in order to estimate the protective potential of the silica shell. After modification by APTES and oxidation with nitric acid, the nonstoichiometric nature of the magnetite nanoparticles according to XRD data increased, which indicates an increase in transition forms compared to the initial sample (magnetite content decreased to 27% and 24%, respectively). In contrast, Mössbauer spectroscopy data detected a decrease in the nonstoichiometric index due to APTES modification conditions, but strong oxidation after exposure to nitric acid. It also showed that by analyzing the data of the diffraction analysis and Mössbauer spectroscopy for the same sample, one can obtain information not only about the ionic composition of “magnetite”, but also about the distribution of iron ions of different charges over the crystalline and amorphous parts of the preparation.

**Keywords:** magnetite nanoparticles; silica-modified magnetite nanoparticles; oxidation degree; amorphous and crystal phases; X-ray analysis; Mössbauer spectroscopy



**Citation:** Dzeranov, A.; Bondarenko, L.; Pankratov, D.; Dzhardimalieva, G.; Jorobekova, S.; Saman, D.; Kydralieva, K. Impact of Silica-Modification and Oxidation on the Crystal Structure of Magnetite Nanoparticles. *Magnetochemistry* **2023**, *9*, 18. <https://doi.org/10.3390/magnetochemistry9010018>

Academic Editor: Andrea Caneschi

Received: 28 November 2022

Revised: 28 December 2022

Accepted: 30 December 2022

Published: 2 January 2023



**Copyright:** © 2023 by the authors. Licensee MDPI, Basel, Switzerland. This article is an open access article distributed under the terms and conditions of the Creative Commons Attribution (CC BY) license (<https://creativecommons.org/licenses/by/4.0/>).

## 1. Introduction

Magnetite Fe<sub>3</sub>O<sub>4</sub> nanoparticles (NPs) are widely studied for their application in various fields of biomedicine, including drug delivery systems [1]; protein purification [2]; as a suitable platform to control the release of nucleic acids in gene therapy [3]; as contrast agents for magnetic resonance imaging [4]; and for catalytic applications, such as the Fenton reaction [5] etc., due to their small size [6], high surface area to volume ratio [7], surface modification capability [8], and high magnetic properties [9].

Many studies emphasize the importance of understanding the transformations of nanomaterials after they enter the real environment, such as aggregation, dissolution, redox reactions, and interactions with macromolecules, which ultimately change their fate, transportation, and potential toxicity [10–14]. Different morphologies and compositions have been observed when iron nanoparticles are oxidized, ranging from iron/iron oxide core-shell structures [15] to iron/iron oxide core-void-shell structures, iron oxide solid spheres, or even iron-based hollow structures [16,17]. For instance, it has been reported that the structure and composition of aged nano zero-valent iron (nZVI) varied considerably depending on the iron type (e.g., FeH<sub>2</sub>, produced by hydrogen reduction of ferric

oxides, and FeBH, prepared using a borohydride reduction method), solution composition, solution pH, dissolved oxygen, temperature, and so on [18–20]. Dong et al. 2016, Xie et al., 2017a, and Dong et al., 2017b. [21–23] showed that magnetite ( $\text{Fe}_3\text{O}_4$ ) and/or maghemite ( $\gamma\text{-Fe}_2\text{O}_3$ ) are the dominant corrosion products of bare nZVI after 90 days of aging, while the crystalline lepidocrocite ( $\gamma\text{-FeOOH}$ ) is the primary end product of aging of nZVI coated with carboxymethyl cellulose. Correspondingly, various kinds of structures (spherical, needle-like, sheet-like, and plate-like) were found during the aging time [21–25]. The differences in morphology and composition could be attributed to the geochemical conditions (solution composition, pH, ORP), the preparation method of the nanoparticles (FeBH and  $\text{FeH}_2$ , produced by the borohydride reduction method and the hydrogen reduction method, respectively), and the aging time [19,25–27]. Dong et al., 2018 [28] demonstrated that Fe/Ni NPs transformed from nanoscale spherical particles to larger-sized flaky-like and needle-like oxides with aging time, and that Fe0 rapidly disappeared and magnetite ( $\text{Fe}_3\text{O}_4$ ) and/or maghemite ( $\gamma\text{-Fe}_2\text{O}_3$ ) were the main aging products.

In the case of  $\text{Fe}_3\text{O}_4$ , it has multiple vacancies and abundant divalent iron atoms, making it easy to transform it into a high oxidation degree by the mechanism of the iron cations diffusion [29–31]. After oxidation of  $\text{Fe}_3\text{O}_4$ , its magnetic properties are greatly reduced [32,33]. Thus, Schwaminger et al. [32] simulated the process of oxidation of magnetite NPs in hard (0.07 mol/L  $\text{HNO}_3$ ) and soft (60 °C, air atmosphere) oxidation conditions and showed that in 24 h, not only the hard conditions, but also the soft conditions, led to a complete phase transformation of magnetite into maghemite ( $\gamma\text{-Fe}_2\text{O}_3$ ). Tombácz et al., 2007 [34], showed that transformation of magnetite during long-term aging in water to maghemite and the formation of an akageneite shell on the magnetic core, as well as a slight increase in particle size, were proven to cause no change in the superparamagnetic features of nanoparticles after storage over the course of 6 years.

Thus, most studies ignore the change in the phase composition of iron nanoparticles under changing environmental conditions (pH,  $\text{O}_2$ , UV radiation, etc.). In turn, a change in the oxidation state, i.e., in particular, the oxidation of the surface of  $\text{Fe}_3\text{O}_4$  nanoparticles to  $\text{Fe}_2\text{O}_3$ , will lead to a change in biological responses [35]. Since the surface characteristics stand out as one of the most important, if not the main, determining factor of biological activity, the surface of nanoparticles appears to be the most noticeable and early impact point to consider [36].

Therefore, an additional protective shell on the surface is required to prevent oxidation, aggregation, and sedimentation of magnetic nanoparticles [37,38]. It demonstrates a possibility to design efficient chemical procedures to attach polymer chains (such as polyethylene glycol or PEG) to improve the biocompatibility of the magnetite nanoparticles [39]. The increase of biocompatibility of these magnetic nanoparticles can significantly contribute to preventing the non-desirable toxic side effect by the patients in drug delivery therapies [40]. Successful modification of  $\text{Fe}_3\text{O}_4$  nanoparticles with various silicas as a protective shell have been reported in many works [41–43]. For example, the use of tetraethoxysilane (TEOS), as a silica derivative, leads to the formation of strong covalent bonds between  $\text{Fe}_3\text{O}_4$  NPs, stability under acidic conditions, and inertness to redox reactions [44–46]. (3-Aminopropyl) triethoxysilane (APTES) is an important amino silane coupling agent and is widely used to promote interfacial behavior of various inorganic oxides, including  $\text{Fe}_3\text{O}_4$  [47,48]. Various applications of magnetite-alkoxysilane nanoparticles are known, such as detoxifying agents in environmental control [49,50], drug delivery systems [51–53], agents for hyperthermia and electrochemical sensing of biologically active compounds [54], agents for MR imaging application [55], etc. However, no works have been found confirming the stability of magnetite nanoparticles modified with silanes under the oxidative effect of the environment. Thus, the question of the phase stability of magnetite nanoparticles coated with a protective shell when exposed to various environmental factors, such as oxygen, biota, etc., remains open. Previously, there were no reports on the estimation of stability of crystalline structures of iron oxides with a protective shell in any oxidation simulating experiments.

The present study aims to investigate the effect of modifying magnetite nanoparticles with 3-aminopropyltriethoxysilane in their phase state during oxidation (by exposure to nitric acid). The crystal structure and composition of magnetite nanoparticles (MNPs) have been examined by X-ray diffraction as well Mössbauer spectroscopy.

## 2. Materials and Methods

### 2.1. Materials

Reagents included  $\text{FeCl}_3 \cdot 6\text{H}_2\text{O}$  (Brom, Russia),  $\text{FeCl}_2 \cdot 4\text{H}_2\text{O}$  (Altayskiy Khimprom, Russia), ammonium hydroxide (Altayskiy Khimprom, Russia), 3-aminopropyltriethoxysilane (APTES, 98%, Sigma-Aldrich, USA), ethanol, and nitric acid (0.07 M  $\text{HNO}_3$ , Azot, Russia). All reagents for experiments were chemically graded and used without further purification. All solutions and dilutions were prepared in deionized water.

### 2.2. Synthesis of $\text{Fe}_3\text{O}_4$

The bare  $\text{Fe}_3\text{O}_4$  MNPs was prepared by the coprecipitation method, which has been described previously [56]. In brief, 7.6 g of  $\text{FeCl}_3 \cdot 6\text{H}_2\text{O}$  and 2.8 g of  $\text{FeCl}_2 \cdot 4\text{H}_2\text{O}$  were dissolved in 70 mL  $\text{H}_2\text{O}$ . Then, 40 mL of 25% of  $\text{NH}_4\text{OH}$  was added at 50 °C under an argon flow with vigorous stirring at 1200 rpm using a rotating agitator. The  $\text{Fe}_3\text{O}_4$  synthesized nanoparticles were washed with ultrapure water five times to remove the synthesis residues, then dried at 70 °C under a vacuum.

### 2.3. Synthesis of $\text{Fe}_3\text{O}_4$ -APTES MNPs

The synthesis of the silica-coated magnetite nanoparticles was carried out by the well-known Stöber method [57]. The previously synthesized magnetite nanoparticles were used as cores to be coated with  $\text{SiO}_2$ . 3-aminopropyltriethoxysilane (APTES) was used as the  $\text{NH}_2$ -silica precursor. According to [58], 3.2 g of  $\text{Fe}_3\text{O}_4$  MNPs was dispersed in 150 mL of ethanol/water (volume ratio, 1:1) solution. Then, 13.6 g of APTES was added to the solution under an argon atmosphere at 40 °C for 2 h. The molar ratio of APTES to  $\text{Fe}_3\text{O}_4$  was used at 4:1. The room temperature cooled solution of the formulated  $\text{Fe}_3\text{O}_4$ -APTES MNPs was separated with a Nd-magnet (0.3 T). To avoid the occurrence of nonspecifically bound silane to the particle surfaces, all subsequent silanization reactions were performed in 1:1 mixtures of ethanol:water and extensively washed with water before analysis or further use. Finally, the  $\text{Fe}_3\text{O}_4$ -APTES were vacuum-dried at 70 °C for 2 h.

### 2.4. Oxidation of MNPs

To assess the stability of the crystal structure and composition of silica-coated nanoparticles to oxidative action, the oxidation treatment was simulated and adopted from Schwaminger [32], but for bare NPs. Nitric acid was utilized as strong oxidizing agent according to [32]. One-hundred-milliliters of the  $\text{Fe}_3\text{O}_4$  (1.2 g)-nitric acid (490 mmol) suspension was stirred at 150 rpm and stored at 40 °C for 24 h in the light. Then, the precipitate was washed three times with deionized water and dried at 70 °C during 2 h in the thermostat.

In total, three samples were investigated: bare magnetite  $\text{Fe}_3\text{O}_4$ ,  $\text{Fe}_3\text{O}_4$ -APTES, and  $\text{Fe}_3\text{O}_4$ -APTES ox (after oxidation), referred to further as M, MA, and MAox, respectively.

### 2.5. Characteristics of the NPs Microstructure

The phase composition and primary particle size of the samples were determined by X-ray diffraction analysis (XRD) in the Bragg–Brentano geometry using a Philips X-pert diffractometer (Philips Analytical, Eindhoven, The Netherlands,  $\text{Cr}_{K\alpha 1}$  radiation,  $\lambda = 2.28976 \text{ \AA}$ ). The experimental data were smoothed with the well-known algorithm by A. Savitzky and M.J.E. Golay (described in [59], corrected by Steinier, Termonia, and Deltour in [60]). The measurements were performed at room temperature in the angular range of  $10^\circ < 2\Theta < 110^\circ$  with  $0.025^\circ$  resolution and exposure for 1 s.

Quantitative analyses were performed by refinement of the total multiphase spectrum method (the Rietveld method) with a fundamental parameters approach [61] using the

Match! software. The full width at half maximum (FWHM) was used for particle size determination with the Scherrer equation [62] using Match! software.

Mössbauer spectra were obtained on a MS1104EM spectrometer (ZAO Kordon, Rostov-on-Don, Russia) with  $^{57}\text{Co}/\text{Rh}$  (RITVERC JSC St. Petersburg, Russia) activity of 1–5 mCi as a source of  $\gamma$ -radiation. The spectra were recorded for each sample both at room temperature and at the boiling point of liquid nitrogen in an evacuated cryostat. The temperature control accuracy of the samples was  $\pm 2$  and  $\pm 0.5$  deg, respectively. The spectra were obtained in high resolution (1024 points) with a noise:signal ratio of less than 1%. Experimental data were processed using software and Spectr Relax 2.8 (MSU, Moscow, Russia). The values of chemical shifts in the manuscript are given relative to  $\alpha$ -Fe.

### 3. Results and Discussion

The diffraction patterns of samples M, MA, and MAox contain eight intense and broadened diffraction reflections, which were slightly different in position and width (Figure 1) with Miller indices (111,  $\sim 27^\circ$ ), (220,  $\sim 45^\circ$ ), (311,  $\sim 54^\circ$ ), (222,  $\sim 56^\circ$ ), (400,  $\sim 66^\circ$ ), (422,  $\sim 84^\circ$ ), (511,  $\sim 90^\circ$ ), and (440,  $\sim 101^\circ$ ) [JCPDS-ICDD 19-629]. Experimental data are described using a curve calculated by the Rietveld method. The various curves show the difference between the calculated and experimental data.

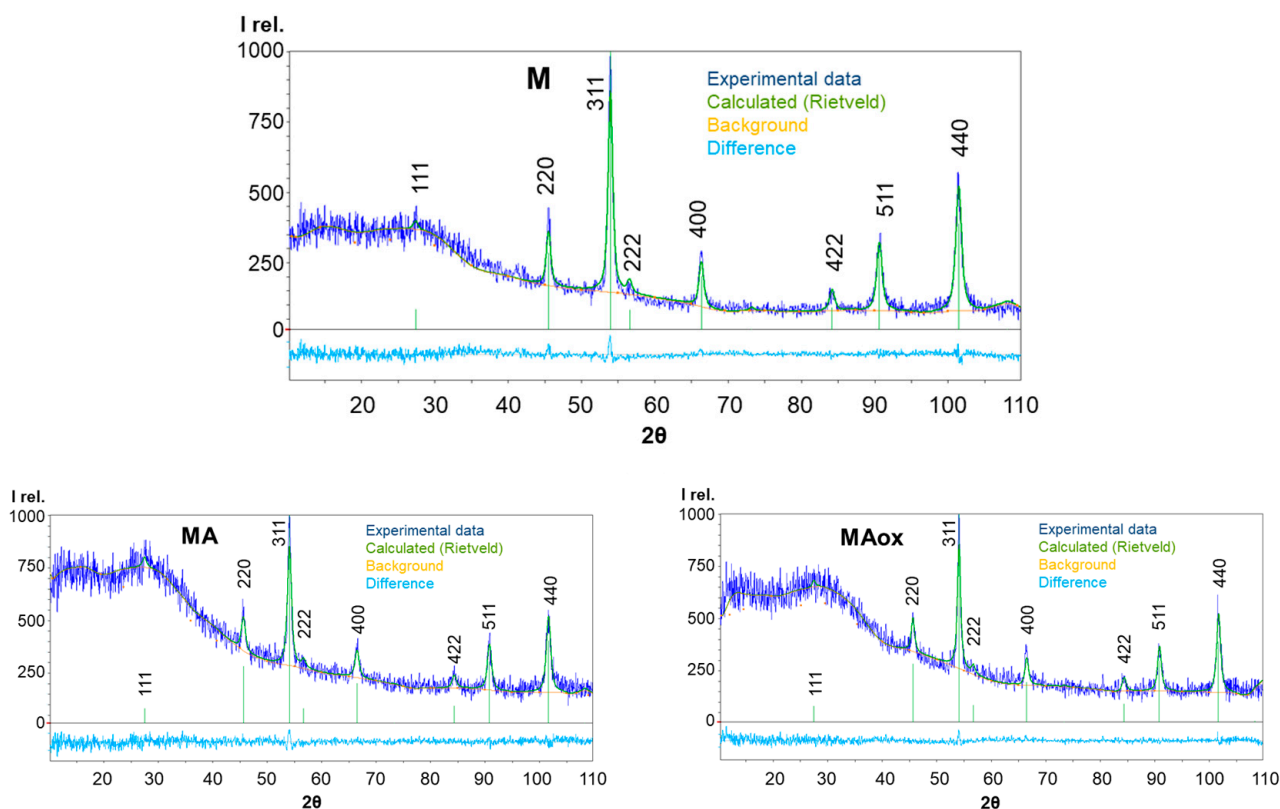


**Figure 1.** Experimental diffraction patterns of samples M, MA, MAox, and the results of their refinement by the Rietveld method.

Quantitative analysis by the Rietveld method shows that all diffraction patterns can be interpreted as describing a single phase with a face-centered cubic ( $Fd\bar{3}m$ ) lattice. The lattice parameters calculated from the diffraction data for the studied samples are presented in Table 1. In addition, Table 1 shows the values of the parameter  $\chi^2$  used as the Rietveld error index, which can be determined from the ratio of the predicted and weighted R-factors of the profile  $\chi^2 = (R_{WP}/R_{exp})^2$  [63]. According to [63], a value of  $\chi^2$  close to 1 is considered satisfactory (Figure 1).

**Table 1.** Rietveld quantitative analysis and magnetite content (%).

| Sample                                    | M                            | MA                           | MAox                         |
|---|------------------------------|------------------------------|------------------------------|
| $a^1$ , Å                                 | $8.3643 \pm 0.0003$          | $8.3531 \pm 0.0003$          | $8.3511 \pm 0.0004$          |
| $\chi^2$                                  | 1                            | 0.8                          | 0.8                          |
| X   | 0.22                         | 0.12                         | 0.1                          |
| $\delta$                                  | 0.16                         | 0.23                         | 0.25                         |
| $x_{\text{Fe}_3\text{O}_4}$ , %           | 51.3                         | 27.3                         | 24.2                         |
| $\text{Fe}_{3-\delta}\text{O}_4$ compound | $\text{Fe}_{2.84}\text{O}_4$ | $\text{Fe}_{2.76}\text{O}_4$ | $\text{Fe}_{2.75}\text{O}_4$ |
| $D_{\text{XRD}}$ , nm                     | $21.7 \pm 0.1$               | $20.9 \pm 0.2$               | $23.3 \pm 1.9$               |

<sup>1</sup>  $a$ —lattice parameter, Å;  $\chi^2$ —weighted ratio of profile R-factors; X—ratio  $\text{Fe}^{2+}/\text{Fe}^{3+}$  or degree of stoichiometry;  $\delta$ —“ $\delta$  in  $\text{Fe}_{3-\delta}\text{O}_4$ ”—parameter of non-stoichiometric nano-magnetite [64];  $x_{\text{Fe}_3\text{O}_4}$ —magnetite content (%), calculated according to [65]; compound  $\text{Fe}_{3-\delta}\text{O}_4$ —composition of partially oxidized magnetite;  $D_{\text{XRD}}$ —the average size of the coherent scattering region calculated using the Scherrer equation.

According to Gorski [65] and Frison [66], the data in Table 1 shows the composition and the content of stoichiometric  $\text{Fe}_3\text{O}_4$ , which varies from 51.3 to 24.2% for the bare magnetite and its modification with APTES and nitric acid. The lattice parameters of the bare and modified NPs are smaller than those of magnetite [JCPDS-ICDD 19-629], but larger than those of maghemite [JCPDS-ICDD 39-1346]. This phenomenon is explained by the partial oxidation of iron(II) ions during drying and storage in the case of the initial magnetite [67]. The size of the region of coherent scattering of nanoparticles  $D_{\text{XRD}}$  was obtained from powder X-ray diffraction data using the Scherrer method (Table 1).

APTES modification of magnetite nanoparticles leads to an increase in the degree of oxidation of NPs: thus, the stoichiometry of the initial magnetite  $\text{Fe}_{2.84}\text{O}_4$  changes to  $\text{Fe}_{2.76}\text{O}_4$ , which correlates with our previous paper where we first calculated the magnetite content in a magnetite-maghemite mixture for functionalized particles [68]. At the same time, the effect of nitric acid on the MA sample did not lead to oxidation, which indicates the efficiency of APTES modification; this was not observed for bare magnetite nanoparticles in Schwaminger’s experiments with nitric acid [32] and confirms the strength of the Fe-O-Si covalent bond between the surface groups of magnetite and the silanol groups of APTES [48,69].

The XRD method does not allow one to accurately distinguish between magnetite and maghemite due to the superposition of peaks in the diffraction patterns [70]. Mössbauer spectroscopy is a powerful tool for identifying both the electronic state of iron atoms and the composition and geometry of their immediate environment in various compounds. Therefore, one can expect the registration of differences in physicochemical properties for relatively similar nanoparticles of maghemite and magnetite [32,71].

Mössbauer spectra at room temperature in all samples demonstrate the form of distorted asymmetrically broadened sextets (Figure 2). The sextets are not symmetrical, both in intensity and in width.

For example, in sample M 1–3, the resonance lines have a noticeably larger width and lower intensity than lines 4–6 (Figure 2). The line intensities are the same within groups 1–2 and 5–6. The spectrum of the MA sample has similar features, differing in a slightly smaller width of all lines and the presence of weak “shoulders” on the inner sides of lines 1 and 2, indicating a greater inhomogeneity of the local environments of iron atoms in the sample. On the contrary, the MAox sample, in contrast to the M sample, differs in a slightly wider resonance line width; the differences in intensity in pairs 1, 6 and 2, 5 are practically leveled out, and in the line widths they are not observed at all. At the same time, the intensity of lines 2 and 5 increased significantly to the extent that it noticeably exceeded the intensity of lines 1 and 6.

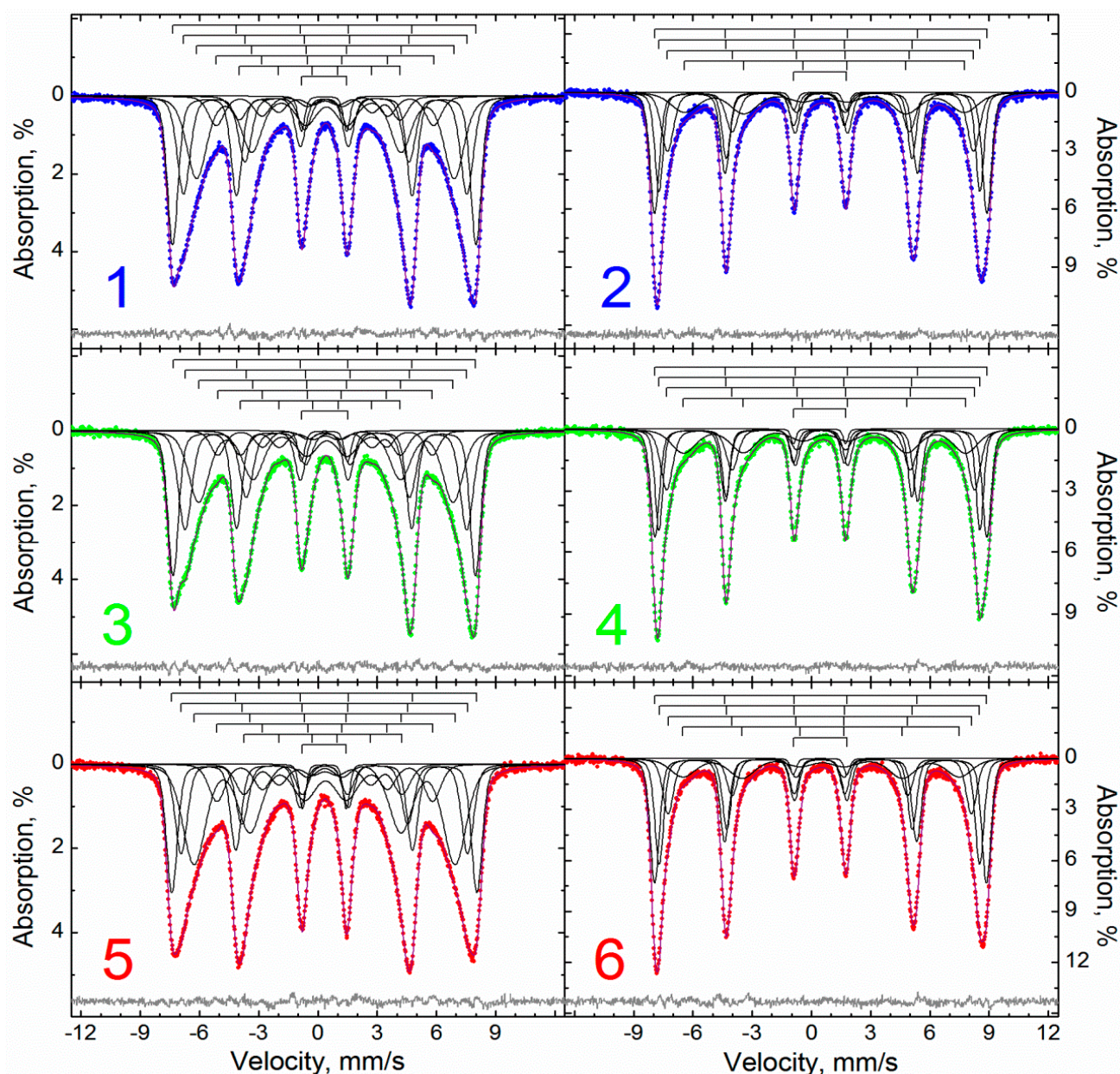


**Figure 2.** Description of the Mössbauer spectra within the framework of the “classical model” of samples: 1, 3, 5—M, MA, MAox measured at 295 K, and 2, 4, 6—M, MA, MAox measured at 78 K.

Lowering the temperature to 78 K leads to a significant increase in intensity expected for nanoobjects, a decrease in the width of resonance lines, and an increase in their symmetry (Figure 2). The intensity ratio of the lines also changes; for samples M and MA, the first resonance line is noticeably more intense and narrower than the sixth one; the second line is slightly more intense; and the fifth, third, and fourth lines are close in intensity. Similar changes are also observed for the MAox sample, with the only difference being that the relaxation distortion of its sextets is much smaller than that of the predecessors.

All spectra, similar to [72], can be satisfactorily described within a single model of five (295 K) or four (78 K) nested symmetrical sextets and one symmetrical doublet (Table 2). In general, the models for different samples are similar to each other, and differ mainly in the ratio of the contributions of each of the subspectra for an individual sample. Thus, in high-temperature spectra, the first, second, and third sextets have the largest areas.

**Table 2.** Results of a model description of the Mössbauer spectra of samples of  $\text{Fe}_{3-\delta}\text{O}_4$ .

| Temperature, K |            | 295                   |          |                       |                 |    | 78       |          |                       |                 |    |
|----------------|------------|-----------------------|----------|-----------------------|-----------------|----|----------|----------|-----------------------|-----------------|----|
| Sample         | Subspectra | $\delta$ <sup>1</sup> | $\Delta$ | $\Gamma_{\text{exp}}$ | $H_{\text{hf}}$ | S  | $\delta$ | $\Delta$ | $\Gamma_{\text{exp}}$ | $H_{\text{hf}}$ | S  |
|                |            |                       | mm/s     |                       | κOe             | %  |          | mm/s     |                       | κOe             | %  |
| M              | 1          | 0.33                  | 0.00     | 0.65                  | 476.7           | 30 | 0.49     | −0.02    | 0.56                  | 522.3           | 33 |
|                | 2          | 0.42                  | −0.08    | 0.77                  | 445.3           | 23 | 0.40     | 0.01     | 0.50                  | 504.3           | 24 |
|                | 3          | 0.41                  | −0.05    | 1.19                  | 405             | 30 | 0.47     | −0.01    | 0.74                  | 481.0           | 21 |
|                | 4          | 0.36                  | 0.00     | 0.94                  | 342             | 9  | 0.67     | −0.02    | 1.62                  | 440             | 19 |
|                | 5          | 0.23                  | −0.28    | 0.92                  | 253             | 6  |          |          |                       |                 |    |
|                | 6          | 0.32                  | 2.28     | 0.40                  |                 | 2  | 0.44     | 2.67     | 0.38                  |                 | 2  |
| MA             | 1          | 0.32                  | 0.00     | 0.64                  | 475.1           | 30 | 0.50     | −0.03    | 0.54                  | 521.6           | 30 |
|                | 2          | 0.46                  | −0.10    | 0.79                  | 442.6           | 26 | 0.39     | 0.02     | 0.46                  | 504.4           | 24 |
|                | 3          | 0.43                  | −0.04    | 1.22                  | 400             | 28 | 0.48     | −0.03    | 0.73                  | 483.7           | 23 |
|                | 4          | 0.35                  | 0.02     | 0.84                  | 337.0           | 7  | 0.68     | −0.03    | 1.47                  | 443             | 22 |
|                | 5          | 0.25                  | −0.26    | 0.92                  | 251             | 7  |          |          |                       |                 |    |
|                | 6          | 0.34                  | 2.35     | 0.42                  |                 | 2  | 0.42     | 2.64     | 0.28                  |                 | 1  |
| MAox           | 1          | 0.33                  | 0.00     | 0.66                  | 479.2           | 23 | 0.47     | 0.00     | 0.56                  | 521.3           | 35 |
|                | 2          | 0.34                  | −0.03    | 0.73                  | 450.0           | 18 | 0.41     | −0.01    | 0.53                  | 503.4           | 28 |
|                | 3          | 0.36                  | −0.04    | 1.36                  | 410             | 37 | 0.43     | 0.00     | 0.65                  | 476.5           | 18 |
|                | 4          | 0.35                  | 0.01     | 0.98                  | 338.7           | 10 | 0.52     | −0.05    | 1.51                  | 435             | 17 |
|                | 5          | 0.31                  | −0.09    | 1.00                  | 248.3           | 8  |          |          |                       |                 |    |
|                | 6          | 0.33                  | 2.23     | 0.40                  |                 | 3  | 0.45     | 2.72     | 0.35                  |                 | 3  |

<sup>1</sup>  $\delta$ —isomeric shift,  $\Delta$ —quadrupole splitting,  $\Gamma_{\text{exp}}$ —line width,  $H_{\text{hf}}$ —hyperfine magnetic field and S—relative subspectrum area.

In low-temperature spectra, subspectra 1 and 2 have the largest areas, while the areas of subspectra 3 and 4, that are close to each other with samples M and MA, do not differ in the high-temperature spectrum much from the area of subspectrum 2. These features, which characterize the distribution of iron atoms in crystallographic positions with different degrees of ordering of the local environment, distinguish these samples from “magnetite” from [72], for which, in addition to the outer sextet (similar to subspectrum 1), one of the “inner” sextets (similar to subspectrum 4) had the largest area, and the areas in the low-temperature spectrum decreased monotonically from outer to internal.

The hyperfine parameters of the subspectra of samples M and MA are close at both temperatures. At the same time, based on data at room temperature, all sextets can be divided into three groups. The first combines subspectra 1 and 4 (Table 2) with isomeric shifts corresponding to iron (+3) atoms in an octahedral oxygen environment [73]. The second group contains subspectrum 5 with an isomeric shift corresponding to iron (+3) atoms in a tetrahedral oxygen environment [73].

Finally, subspectra 2 and 3, which have too high isomeric shifts for iron atoms (+3) (in an octahedral environment), but too small for iron atoms (+2.5) in octahedral voids of magnetite [74], refer to iron atoms in the octahedral voids of the oxidized form of nanomagnetite— $\text{Fe}_{3-\delta}\text{O}_4$ , in which the proportion of iron (+3) significantly exceeds the proportion of iron (+2). At low temperatures, the sextets rearrange (due to the Verwey transition) but can also be separated into iron (+3) and partially reduced atoms (Table 2, 78 K, subspectra 1–3 and 4, respectively).

The values of magnetic splittings determined at room temperature are expected to be less for bulk samples of magnetite and maghemite [75], which is typical for nanosized ma-

materials [76]. As the temperature drops to 78 K, the outer sextet reaches a value characteristic of one of the bulk magnetite sextets [74].

The isomeric shifts of all MAox subspectra obtained at room temperature indicate that all iron atoms were oxidized to the oxidation state (+3) (octahedral positions). Even at 78 K, the isomer shift of sextet 4 decreased significantly (Table 2). Otherwise, the Mössbauer parameters did not undergo significant changes, except for a noticeable increase in the widths of almost all subspectra, which may be associated with a decrease in particle size after the acid treatment.

The probability functions of the distribution of magnetic fields obtained for low-temperature Mössbauer spectra for all samples have the form of asymmetric unimodal peaks strongly shifted in the region of high fields (Figure 3). Their parameters do not differ from each other practically, except for the fact that the MA distribution maximum is located at a slightly smaller field value (Table 3).

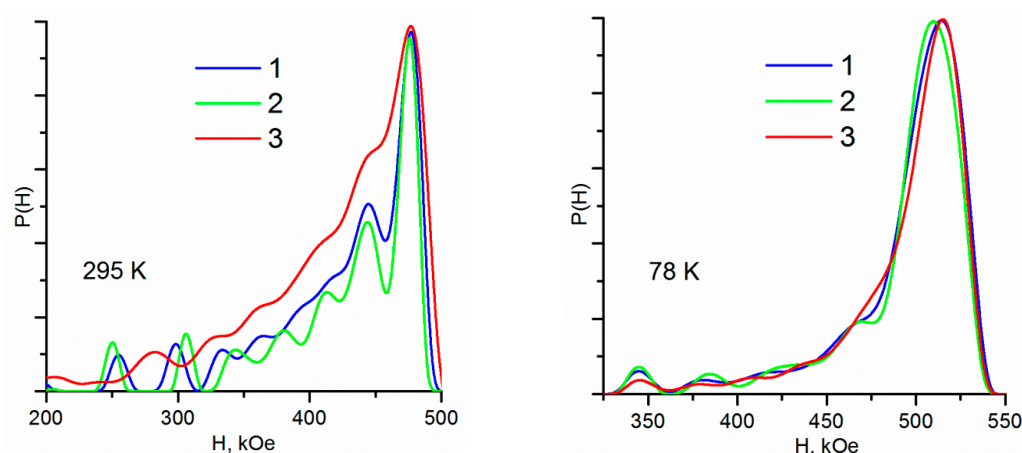


**Figure 3.** Probability functions of the distribution of magnetic fields at different sample temperatures: 1—M, 2—MA, 3—MAox.

The probability functions of the distribution of hyperfine parameters for high-temperature spectra differ for different samples. Thus, for sample M, the field distribution form appears as a predominantly asymmetric two-modal peak with maxima localized in the region of high fields and an extended “wing” stretches into low fields (Figure 3). In MA (with the same predominant asymmetric two-modal peak), this wing is a little more resolved—three local maxima are clearly manifested on it.

Prior to the beginning of this “wing” in the region of 255 and 300 kOe, two weak “satellites” are observed for both samples. In MAox, in contrast to its predecessors, there is practically no “fine structure” on the probability dependence of the distribution of magnetic fields—the distribution has the form of a noticeably wider unimodal peak, with a mean value shifted to lower fields (Table 3). This indicates a much wider size distribution of MAox particles (with a variety of local environments).

The reason for distortions of the relaxation nature of the Mössbauer spectra of the samples is the small size of the iron-containing domains, which makes it possible to consider the description of the spectra in terms of the model of multilevel superparamagnetic relaxation [77] (Table 3, Figure 4). In this case, the samples can be satisfactorily described within the framework of a single model of two and three relaxation sextets for high-temperature and low-temperature spectra, respectively.

**Table 3.** Results of the description of the Mössbauer spectra of the samples  $\text{Fe}_{3-\delta}\text{O}_4$  using the distribution function of magnetic fields ( $P(H)$ ) and within the framework of the multilevel superparamagnetic relaxation (MSSPR) model.

| Spectra Description Method |             | P(H)                                     |  |          | MSSPR    |                  |                   |          |    |       |
|----------------------------|-------------|--|--|----------|----------|------------------|-------------------|----------|----|-------|
| Sample                     | Temperature | $H_{\text{max}}^{\text{d}}$ <sup>1</sup> | $H_{\text{w}}^{\text{d}} \pm \sqrt{D}$ | $\delta$ | $\Delta$ | $G_{\text{exp}}$ | $H_{\text{hf}}$   | $\alpha$ | S  | d     |
|                            | K           | $\kappa\text{Oe}$                        | $\kappa\text{Oe}$                      |          | mm/s     |                  | $\kappa\text{Oe}$ |          | %  | nm    |
| M                          | 295         | 476.3                                    | $415 \pm 78$                           | 0.31     | 0.02     | 0.46             | 482.8             | 4.78     | 88 | 15.49 |
|                            |             |  |  | 0.75     | 0.16     | 0.33             | 465.6             |          | 12 |       |
|                            | 78          | 512.6                                    | $482 \pm 71$                           | 0.49     | 0.02     | 0.40             | 526.9             | 18.1     | 39 |       |
|                            |             |  |  | 0.63     | 0.00     | 1.00             | 461.2             |          | 18 |       |
| MA                         | 295         | 477.3                                    | $414 \pm 79$                           | 0.31     | 0.03     | 0.44             | 482.2             | 4.91     | 83 | 15.63 |
|                            |             |  |  | 0.74     | 0.09     | 0.34             | 461.6             |          | 17 |       |
|                            | 78          | 508.4                                    | $481 \pm 69$                           | 0.41     | 0.00     | 0.43             | 507.9             | 18.6     | 44 |       |
|                            |             |  |  | 0.68     | 0.01     | 1.04             | 462.4             |          | 21 |       |
| MAox                       | 295         | 476.6                                    | $409 \pm 82$                           | 0.33     | 0.00     | 0.47             | 485.4             | 4.57     | 82 | 15.27 |
|                            |             |  |  | 0.39     | 0.06     | 0.85             | 439.9             |          | 18 |       |
|                            | 78          | 511.7                                    | $483 \pm 67$                           | 0.47     | 0.00     | 0.40             | 525.8             | 17.3     | 45 |       |
|                            |             |  |  | 0.41     | 0.01     | 0.45             | 507.4             |          | 41 |       |
|                            |             |  |  | 0.47     | 0.01     | 0.84             | 461.1             |          | 14 |       |

<sup>1</sup>  $H_{\text{max}}^{\text{d}}$ ,  $H_{\text{w}}^{\text{d}}$ —the position of the maximum and weighted average for the distribution function of magnetic fields, D—dispersion  $H_{\text{w}}^{\text{d}}$ ,  $\alpha$ —ratio of particle anisotropy energy to thermal energy, d—magnetic domain diameter.

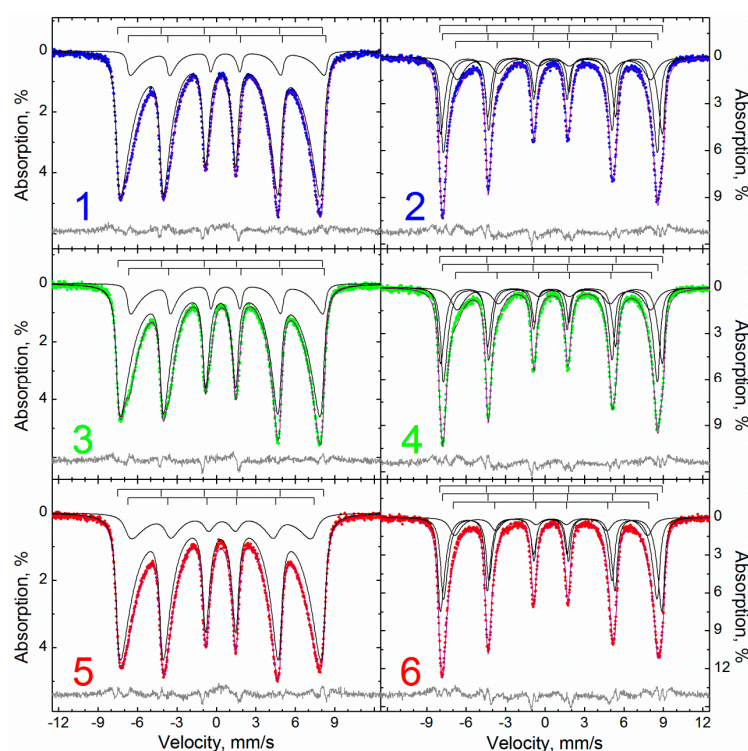


**Figure 4.** Description of the Mössbauer spectra within the model of multilevel superparamagnetic relaxation of the samples: 1, 3, 5—M, MA, MAox measured at 295 K, and 2, 4, 6—M, MA, MAox measured at 78 K.

The spectra obtained at different temperatures were interconnected by the parameter  $\alpha$  equal to the ratio of the particle anisotropy energy to the thermal energy:

$$\alpha = \frac{KV}{k_B T} \quad (1)$$

where  $K$  is the magnetic anisotropy constant,  $V$  is the domain volume,  $k_B$  is the Boltzmann constant, and  $T$  is the temperature. It was assumed that  $K$  does not depend on the temperature, i.e., the product  $\alpha$ .  $T$  was taken as a constant value for each sample. Based on this parameter, using a simplified model of spherical particles, and an average value of the magnetic anisotropy constant given in the literature for maghemite and magnetite (104 J/m<sup>3</sup> [78,79]), the sizes of magnetic domains were estimated (Table 3).

In the spectra obtained at both temperatures, iron atoms located in different crystallographic positions are quite distinguishable within the framework of the relaxation model: at room temperature, two sublattices occur, iron (+3) and mixed-valent iron (for samples M and MA). Below the Verwey temperature, due to the ordering of atoms in the magnetic sublattices of iron, it becomes necessary to use three relaxation subspectra to describe low-temperature spectra.

At the same time, the corresponding parameters of the M and MA samples differ little from each other, while the data of the MAox sample is most distinguished by the absence of subspectra with high isomeric shifts (i.e., corresponding to iron atoms in low oxidation states).

Using the data in Tables 2 and 3, it is possible to estimate the nonstoichiometric parameter  $\delta$  for the studied samples. To do this, it is necessary to determine the ratio of the content of Fe<sup>2+</sup> and Fe<sup>3+</sup> ions ( $X_{ms}$ ) in Fe<sub>3- $\delta$</sub> O<sub>4</sub> [64]. It stems from the formula for nonstoichiometric magnetite (Fe<sup>3+</sup>)<sub>A</sub>(Fe<sup>2+</sup><sub>1-3 $\delta$</sub> Fe<sup>3+</sup><sub>1+2 $\delta$</sub> # $\delta$ )<sub>B</sub>O<sub>4</sub> that if Fe<sup>3+</sup> ions are located both in tetrahedral and octahedral positions of the spinel structure (sites A and B, respectively), then Fe<sup>2+</sup> occupies only octahedral positions (B).

The content of iron atoms in certain crystallographic positions can be determined from the experimental Mössbauer spectra, as mentioned above. In the first approximation, it is proportional to the areas of the corresponding subspectra. However, for Fe<sup>2+</sup> and Fe<sup>3+</sup> ions in the octahedral sites of magnetite at temperatures above the Verwey transition, a single resonance signal in the form of a sextet is observed due to the fast electron exchange between them.

It was shown above that the isomeric shift of this sextet can change significantly, which is obviously caused by different ratios of iron ions of different charges in a given crystallographic position. Assuming in the first approximation that the magnitude of this isomeric shift is linear combination of isomeric shifts characterized by Fe<sup>2+</sup> and Fe<sup>3+</sup> ions in an octahedral oxygen environment [80], the desired ratio  $X_{ms}$  can be determined as:

$$X_{ms} = n(\text{Fe}^{2+})/n(\text{Fe}^{3+}) = \sum Q_i \times S_i / \{ \sum (1 - Q_i) \times S_i + \sum S_j \} \quad (2)$$

where  $S_i$ —the relative area of the  $i$ -th subspectra related to atoms “Fe<sup>+2.5</sup>” in B-site,  $S_j$ —the relative area of the remaining subspectra (Fe<sup>+3</sup>), and  $Q_i$  is determined by the formula:

$$Q_i = (\delta_i - \delta + 3) / (\delta + 2 - \delta + 3) \quad (3)$$

where  $\delta_i$  is the isomeric shift of the  $i$ -th subspectrum related to “Fe<sup>+2.5</sup>” atoms in the B-site,  $\delta_{+3}$  is the average value of the isomeric shifts of all subspectra of Fe<sup>3+</sup> atoms in octahedral positions for a given sample at a given temperature, and  $\delta_{+2}$  is the average of the value for isomeric shifts of Fe<sup>2+</sup> atoms in octahedral positions for each of the temperatures, determined by analyzing more than 50 different literature sources [72] ( $\delta_{+2} \approx 1.16$  mm/s for 295 K and 1.33 mm/s for 78 K).

On the basis of the results, a the description of the experimental Mössbauer spectra was obtained, both in the framework of the “classical model” (CM) (a set of symmetrical

sextets, Figure 2, Table 2), and in the framework of the relaxation model (MSSPR) (Figure 4, Table 3). According to the method described above, the quantities  $X_{ms}$  (Equation (2)) were determined, as well as those calculated from them according to the formula [64,71]:

$$\delta = (1 - 2 \times X_{ms}) / (3 + 2 \times X_{ms}) \quad (4)$$

the value of the nonstoichiometric parameter,  $\delta$ , is presented in Table 4.

According to the given data in Table 4, the calculation results align with each other both within each individual model (at different temperatures) and between the two models in general.

**Table 4.** Nonstoichiometry parameters of samples according to Mössbauer spectroscopy data.

| Model          |          | CM       |                    |          |          |                    |          | MSSPR    |                    |          |          |                    |  |
|----------------|----------|----------|--------------------|----------|----------|--------------------|----------|----------|--------------------|----------|----------|--------------------|--|
| Temperature, K |          | 295      |                    | 75       |          | 295                |          | 295      |                    | 295      |          |                    |  |
| Sample         | $X_{ms}$ | $\delta$ | $Fe_{3-\delta}O_4$ |  |
| M              | 0.048    | 0.292    | $Fe_{2.708}O_4$    | 0.051    | 0.289    | $Fe_{2.711}O_4$    | 0.067    | 0.277    | $Fe_{2.723}O_4$    | 0.038    | 0.300    | $Fe_{2.700}O_4$    |  |
| MA             | 0.078    | 0.268    | $Fe_{2.732}O_4$    | 0.062    | 0.281    | $Fe_{2.719}O_4$    | 0.095    | 0.254    | $Fe_{2.746}O_4$    | 0.058    | 0.284    | $Fe_{2.716}O_4$    |  |
| MAox           | 0.009    | 0.325    | $Fe_{2.675}O_4$    | 0.015    | 0.320    | $Fe_{2.680}O_4$    | 0.013    | 0.322    | $Fe_{2.678}O_4$    | 0.004    | 0.329    | $Fe_{2.671}O_4$    |  |

When comparing the obtained results with the diffraction data (Table 1), it is necessary, to mark a noticeable increase in the degree of oxidation, determined in the Mössbauer experiment. The reason for this may be the limitations of XRD methods in relation to the X-ray amorphous phases present in the materials, which are completely detected by Mössbauer spectroscopy. The products of magnetite oxidation should have a low degree of crystallinity, and some of them do not make a significant contribution to the diffraction pattern against the background of reflections from the crystalline part of the material [81].

This is the reason for the underestimation of the degree of oxidation of the material according to XRD data. It follows that the proportion of the X-ray amorphous (and oxidized) part of “magnetite” in the original preparation, M, is significantly higher than in the one that undergoes additional processing and separation, which is MA. Indeed, according to XRD data, the nonstoichiometric parameter,  $\delta$ , for the original preparation M is less than that for MA, while according to Mössbauer spectroscopy, the ratio is reversed. In the sample, M synthesized from the solution, the fraction of the X-ray amorphous phase can be high, and in the MA obtained from it, after a series of manipulations (drying, dispersion, co-precipitation, magnetic separation, etc.), is significantly decreased, which led to the observed differences.

#### 4. Conclusions and Future Perspectives

Analysis of the stoichiometry composition of magnetite nanoparticles after modification by silica and nitric acid (oxidation condition) indicates the appearance of transition forms in comparison to the native sample (magnetite content decreased to 27 wt% and 24 wt%, respectively, according to XRD data). Mossbauer spectroscopy detected a decrease in the nonstoichiometry index in the case of APTES modification, but a strong increase in the index in the case of  $HNO_3$  treatment. Therefore, XRD data, compared with Mössbauer spectroscopy, indicates an underestimation of the degree of oxidation of the material due to the low sensitivity to the X-ray amorphous phase. It is also shown that by analyzing the data of diffraction analysis and Mössbauer spectroscopy for the same sample, one can obtain information not only about the ionic composition of “magnetite”, but also about the distribution of iron ions of different charges over the crystalline and amorphous parts of the preparation. In the future, it would be interesting to study the transformations of magnetic nanoparticles in time and with different morphologies, including rod-shape [82], nanoprisms [83], or square-plate [84], to allow these nanoparticles to be tuned on request.

**Author Contributions:** Conceptualization, K.K. and L.B.; methodology, L.B. and K.K.; software, A.D., D.S. and L.B.; validation, D.P. and G.D.; formal analysis, D.P.; investigation, A.D., L.B. and D.P.; data curation, S.J.; writing—original draft preparation A.D. and D.P.; writing—review and editing, K.K. and L.B.; supervision, G.D. and S.J. All authors have read and agreed to the published version of the manuscript.

**Funding:** This research was funded by Russian Science Foundation, grant number 22-73-10222.

**Institutional Review Board Statement:** Not applicable.

**Informed Consent Statement:** Not applicable.

**Data Availability Statement:** The data presented in this study are available on request from the corresponding author.

**Conflicts of Interest:** The authors declare no conflict of interest.

## References

1. Zhao, X.; Xu, S.; Jiang, Y.; Wang, C.; Rehman, S.U.; Ji, S.; Wang, J.; Tao, T.; Xu, H.; Chen, R.; et al. BSA-magnetite nanotorpedo for safe and efficient delivery of chemotherapy drugs. *Chem. Eng. J.* **2023**, *454*, 140440. [[CrossRef](#)]
2. Hsu, C.-H.; Yu, Y.-S.; Gu, Y.; Wu, K.C.-W. Modification of magnetite-doped NH<sub>2</sub>-MIL-100(Fe) with aliphatic C8 carbon chain for feasible protein purification in reversed-phase mode. *Sep. Purif. Technol.* **2022**, *288*, 120528. [[CrossRef](#)]
3. Prilepskii, A.Y.; Kalnin, A.Y.; Fakharo, A.F.; Anastasova, E.I.; Nedorezova, D.D.; Antonov, G.A.; Vinogradov, V.V. Cationic Magnetite Nanoparticles for Increasing siRNA Hybridization Rates. *Nanomaterials* **2020**, *10*, 1018. [[CrossRef](#)] [[PubMed](#)]
4. German, S.V.; Navolokin, N.A.; Kuznetsova, N.R.; Zuev, V.V.; Inozemtseva, O.A.; Anis'Kov, A.A.; Volkova, E.K.; Bucharskaya, A.B.; Maslyakova, G.N.; Fakhrullin, R.F.; et al. Liposomes loaded with hydrophilic magnetite nanoparticles: Preparation and application as contrast agents for magnetic resonance imaging. *Colloids Surf. B Biointerfaces* **2015**, *135*, 109–115. [[CrossRef](#)] [[PubMed](#)]
5. Thomas, N.; Dionysiou, D.D.; Pillai, S.C. Heterogeneous Fenton catalysts: A review of recent advances. *J. Hazard. Mater.* **2020**, *404*, 124082. [[CrossRef](#)] [[PubMed](#)]
6. Estelrich, J.; Escribano, E.; Queralt, J.; Busquets, M.A. Iron Oxide Nanoparticles for Magnetically-Guided and Magnetically-Responsive Drug Delivery. *Int. J. Mol. Sci.* **2015**, *16*, 8070–8101. [[CrossRef](#)] [[PubMed](#)]
7. Revia, R.A.; Zhang, M. Magnetite nanoparticles for cancer diagnosis, treatment, and treatment monitoring: Recent advances. *Mater. Today* **2016**, *19*, 157–168. [[CrossRef](#)]
8. Yue-Jian, C.; Juan, T.; Fei, X.; Jia-Bi, Z.; Ning, G.; Yi-Hua, Z.; Ye, D.; Liang, G. Synthesis, self-assembly, and characterization of PEG-coated iron oxide nanoparticles as potential MRI contrast agent. *Drug Dev. Ind. Pharm.* **2010**, *36*, 1235–1244. [[CrossRef](#)]
9. Masoudi, A.; Hosseini, H.R.M.; Shokrgozar, M.A.; Ahmadi, R.; Oghabian, M.A. The effect of poly(ethylene glycol) coating on colloidal stability of superparamagnetic iron oxide nanoparticles as potential MRI contrast agent. *Int. J. Pharm.* **2012**, *433*, 129–141. [[CrossRef](#)]
10. Anuchina, M.M.; Pankratov, D.A.; Abroskin, D.P.; Kulikova, N.A.; Gabbasova, D.T.; Matorin, D.N.; Volkov, D.S.; Perminova, I.V. Estimating the Toxicity and Biological Availability for Interaction Products of Metallic Iron and Humic Substances. *Mosc. Univ. Soil Sci. Bull.* **2019**, *74*, 193–198. [[CrossRef](#)]
11. Dwivedi, A.D.; Ma, L.Q. Biocatalytic Synthesis Pathways, Transformation, and Toxicity of Nanoparticles in the Environment. *Crit. Rev. Environ. Sci. Technol.* **2014**, *44*, 1679–1739. [[CrossRef](#)]
12. Lin, D.; Tian, X.; Wu, F.; Xing, B. Fate and Transport of Engineered Nanomaterials in the Environment. *J. Environ. Qual.* **2010**, *39*, 1896–1908. [[CrossRef](#)]
13. Lowry, G.V.; Gregory, K.B.; Apte, S.C.; Lead, J.R. Transformations of Nanomaterials in the Environment. *Environ. Sci. Technol.* **2012**, *46*, 6893–6899. [[CrossRef](#)]
14. Mitrano, D.M.; Motellier, S.; Clavaguera, S.; Nowack, B. Review of nanomaterial aging and transformations through the life cycle of nano-enhanced products. *Environ. Int.* **2015**, *77*, 132–147. [[CrossRef](#)]
15. Carpenter, E.E.; Calvin, S.; Stroud, R.M.; Harris, V.G. Passivated Iron as Core–Shell Nanoparticles. *Chem. Mater.* **2003**, *15*, 3245–3246. [[CrossRef](#)]
16. Wang, C.M.; Baer, D.R.; Thomas, L.E.; Amonette, J.E.; Antony, J.; Qiang, Y.; Duscher, G. Void formation during early stages of passivation: Initial oxidation of iron nanoparticles at room temperature. *J. Appl. Phys.* **2005**, *98*, 094308. [[CrossRef](#)]
17. Pratt, A.; Lari, L.; Hovorka, O.; Shah, A.; Woffinden, C.; Tear, S.P.; Binns, C.; Kröger, R. Enhanced oxidation of nanoparticles through strain-mediated ionic transport. *Nat. Mater.* **2013**, *13*, 26–30. [[CrossRef](#)]
18. Thompson, M.D.K. The Reaction Between Iron and Water in the Absence of Oxygen. *Trans. Electrochem. Soc.* **1940**, *78*, 251–257. [[CrossRef](#)]
19. Reinsch, B.C.; Forsberg, B.; Penn, R.L.; Kim, C.S.; Lowry, G.V. Chemical Transformations during Aging of Zerovalent Iron Nanoparticles in the Presence of Common Groundwater Dissolved Constituents. *Environ. Sci. Technol.* **2010**, *44*, 3455–3461. [[CrossRef](#)]

20. Filip, J.; Karlický, F.; Marušák, Z.; Lazar, P.; Černík, M.; Otyepka, M.; Zbořil, R. Anaerobic Reaction of Nanoscale Zerovalent Iron with Water: Mechanism and Kinetics. *J. Phys. Chem. C* **2014**, *118*, 13817–13825. [[CrossRef](#)]
21. Dong, H.; Zhao, F.; Zeng, G.; Tang, L.; Fan, C.; Zhang, L.; Zeng, Y.; He, Q.; Xie, Y.; Wu, Y. Aging study on carboxymethyl cellulose-coated zero-valent iron nanoparticles in water: Chemical transformation and structural evolution. *J. Hazard. Mater.* **2016**, *312*, 234–242. [[CrossRef](#)] [[PubMed](#)]
22. Xie, Y.; Dong, H.; Zeng, G.; Tang, L.; Jiang, Z.; Zhang, C.; Deng, J.; Zhang, L.; Zhang, Y. The interactions between nanoscale zero-valent iron and microbes in the subsurface environment: A review. *J. Hazard. Mater.* **2017**, *321*, 390–407. [[CrossRef](#)] [[PubMed](#)]
23. Dong, H.; Zhao, F.; He, Q.; Xie, Y.; Zeng, Y.; Zhang, L.; Tang, L.; Zeng, G. Physicochemical transformation of carboxymethyl cellulose-coated zero-valent iron nanoparticles (nZVI) in simulated groundwater under anaerobic conditions. *Sep. Purif. Technol.* **2017**, *175*, 376–383. [[CrossRef](#)]
24. Greenlee, L.F.; Torrey, J.D.; Amaro, R.L.; Shaw, J.M. Kinetics of Zero Valent Iron Nanoparticle Oxidation in Oxygenated Water. *Environ. Sci. Technol.* **2012**, *46*, 12913–12920. [[CrossRef](#)] [[PubMed](#)]
25. Liu, A.; Liu, J.; Zhang, W.-X. Transformation and composition evolution of nanoscale zero valent iron (nZVI) synthesized by borohydride reduction in static water. *Chemosphere* **2015**, *119*, 1068–1074. [[CrossRef](#)] [[PubMed](#)]
26. Kim, H.-S.; Kim, T.; Ahn, J.-Y.; Hwang, K.-Y.; Park, J.-Y.; Lim, T.-T.; Hwang, I. Aging characteristics and reactivity of two types of nanoscale zero-valent iron particles (FeBH and FeH<sub>2</sub>) in nitrate reduction. *Chem. Eng. J.* **2012**, *197*, 16–23. [[CrossRef](#)]
27. Sun, G.; Fenglian, F.; Bing, T. Fate of metal-EDTA complexes during ferrihydrite aging: Interaction of metal-EDTA and iron oxides. *Chemosphere*. **2022**, *291*, 132791. [[CrossRef](#)] [[PubMed](#)]
28. Dong, H.; Jiang, Z.; Deng, J.; Zhang, C.; Cheng, Y.; Hou, K.; Zhang, L.; Tang, L.; Zeng, G. Physicochemical transformation of Fe/Ni bimetallic nanoparticles during aging in simulated groundwater and the consequent effect on contaminant removal. *Water Res.* **2018**, *129*, 51–57. [[CrossRef](#)] [[PubMed](#)]
29. Salazar, J.S.; Perez, L.; de Abril, O.; Phuoc, L.T.; Ihiwakrim, D.; Vazquez, M.; Greneche, J.-M.; Begin-Colin, S.; Pourroy, G. Magnetic Iron Oxide Nanoparticles in 10–40 nm Range: Composition in Terms of Magnetite/Maghemite Ratio and Effect on the Magnetic Properties. *Chem. Mater.* **2011**, *23*, 1379–1386. [[CrossRef](#)]
30. Jungcharoen, P.; Pédrot, M.; Choueikani, F.; Pasturel, M.; Hanna, K.; Heberling, F.; Tesfa, M.; Marsac, R. Probing the effects of redox conditions and dissolved Fe<sup>2+</sup> on nanomagnetite stoichiometry by wet chemistry, XRD, XAS and XMCD. *Environ. Sci. Nano* **2021**, *8*, 2098–2107. [[CrossRef](#)]
31. Al-Hakkani, M.F.; Gouda, G.A.; Hassan, S.H. A review of green methods for phyto-fabrication of hematite ( $\alpha$ -Fe<sub>2</sub>O<sub>3</sub>) nanoparticles and their characterization, properties, and applications. *Heliyon* **2021**, *7*, e05806. [[CrossRef](#)] [[PubMed](#)]
32. Schwaminger, S.P.; Bauer, D.; Fraga-García, P.; Wagner, F.E.; Berensmeier, S. Oxidation of magnetite nanoparticles: Impact on surface and crystal properties. *CrystEngComm* **2017**, *19*, 246–255. [[CrossRef](#)]
33. Vikram, S.; Dhakshnamoorthy, M.; Vasanthakumari, R.; Rajamani, A.R.; Rangarajan, M.; Tsuzuki, T. Tuning the Magnetic Properties of Iron Oxide Nanoparticles by a Room-Temperature Air-Atmosphere (RTAA) Co-Precipitation Method. *J. Nanosci. Nanotechnol.* **2015**, *15*, 3870–3878. [[CrossRef](#)] [[PubMed](#)]
34. Tombácz, E.; Illés, E.; Majzik, A.; Jedlovsky-Hajdú, A.; Rideg, N.; Szekeres, M. Ageing in the inorganic nanoworld: Example of magnetite nanoparticles in aqueous medium. *Croat. Chem. Acta* **2007**, *83*, 513–515.
35. Lei, C.; Zhang, L.; Yang, K.; Zhu, L.; Lin, D. Toxicity of iron-based nanoparticles to green algae: Effects of particle size, crystal phase, oxidation state and environmental aging. *Environ. Pollut.* **2016**, *218*, 505–512. [[CrossRef](#)] [[PubMed](#)]
36. Saei, A.; Yazdani, M.; Lohse, S.E.; Bakhtiary, Z.; Serpooshan, V.; Ghavami, M.; Asadian, M.; Mashaghi, S.; Dreaden, E.; Mashaghi, A.; et al. Nanoparticle Surface Functionality Dictates Cellular and Systemic Toxicity. *Chem. Mater.* **2017**, *29*, 6578–6595. [[CrossRef](#)]
37. Liu, J.; Louie, S.M.; Zhao, J.; Gao, X.; Hu, Y. Aggregation of varied organic coated magnetite nanoparticles: Adsorbed mass and thickness of coatings and interactions with natural organic matter. *Sci. Total Environ.* **2022**, *831*, 154976. [[CrossRef](#)] [[PubMed](#)]
38. Schwaminger, S.P.; Schwarzenberger, K.; Gatzemeier, J.; Lei, Z.; Eckert, K. Magnetically Induced Aggregation of Iron Oxide Nanoparticles for Carrier Flotation Strategies. *ACS Appl. Mater. Interfaces* **2021**, *13*, 20830–20844. [[CrossRef](#)] [[PubMed](#)]
39. Suk, J.S.; Xu, Q.; Kim, N.; Hanes, J.; Ensign, L.M. PEGylation as a strategy for improving nanoparticle-based drug and gene delivery. *Adv. Drug Deliv. Rev.* **2016**, *99*, 28–51. [[CrossRef](#)] [[PubMed](#)]
40. Najahi-Missaoui, W.; Arnold, R.D.; Cummings, B.S. Safe Nanoparticles: Are We There Yet? *Int. J. Mol. Sci.* **2020**, *22*, 385. [[CrossRef](#)] [[PubMed](#)]
41. Abbas, M.; Rao, B.P.; Islam, N.; Naga, S.; Takahashi, M.; Kim, C. Highly stable- silica encapsulating magnetite nanoparticles (Fe<sub>3</sub>O<sub>4</sub>/SiO<sub>2</sub>) synthesized using single surfactantless- polyol process. *Ceram. Int.* **2014**, *40*, 1379–1385. [[CrossRef](#)]
42. Gdula, K.; Gładysz-Plaska, A.; Cristóvão, B.; Ferenc, W.; Skwarek, E. Amine-functionalized magnetite-silica nanoparticles as effective adsorbent for removal of uranium(VI) ions. *J. Mol. Liq.* **2019**, *290*, 111217. [[CrossRef](#)]
43. Mokhtar, H.I.; Abdel-Salam, R.A.; Hadad, G.M. A nanocomposite of silica coated magnetite nanoparticles and aniline-anthranilic acid co-polymeric nanorods with improved stability and selectivity for fluoroquinolones dispersive micro solid phase extraction. *J. Chromatogr. B* **2022**, *1206*, 123350. [[CrossRef](#)]
44. Ahmad, I.; Siddiqui, W.A.; Ahmad, T. Synthesis and characterization of molecularly imprinted magnetite nanomaterials as a novel adsorbent for the removal of heavy metals from aqueous solution. *J. Mater. Res. Technol.* **2019**, *8*, 4239–4252. [[CrossRef](#)]

45. Dayana, I.; Sembiring, T.; Tetuko, A.P.; Sembiring, K.; Maulida, N.; Cahyarani, Z.; Setiadi, E.A.; Asri, N.S.; Ginting, M.; Sebayang, P. The effect of tetraethyl orthosilicate (TEOS) additions as silica precursors on the magnetite nano-particles (Fe<sub>3</sub>O<sub>4</sub>) properties for the application of ferro-lubricant. *J. Mol. Liq.* **2019**, *294*, 111557. [[CrossRef](#)]
46. Turrina, C.; Oppelt, A.; Mitzkus, M.; Berensmeier, S.; Schwaminger, S.P. Silica-coated superparamagnetic iron oxide nanoparticles: New insights into the influence of coating thickness on the particle properties and lasioglossin binding. *MRS Commun.* **2022**, *12*, 632–639. [[CrossRef](#)]
47. Zhang, B.; Wang, Y.; Zhang, J.; Qiao, S.; Fan, Z.; Wan, J.; Chen, K. Well-defined 3-Aminopropyltriethoxysilane functionalized magnetite nanoparticles and their adsorption performance for partially hydrolyzed polyacrylamide from aqueous solution. *Colloids Surf. A Physicochem. Eng. Asp.* **2020**, *586*, 124288. [[CrossRef](#)]
48. Mokkarat, A.; Kruanetr, S.; Sakee, U. One-step continuous flow synthesis of aminopropyl silica-coated magnetite nanoparticles. *J. Saudi Chem. Soc.* **2022**, *26*, 101506. [[CrossRef](#)]
49. Szultka-Młyńska, M.; Al-Suod, H.; Buszewski, B. Inorganic oxide and chemically bonded sorbents. In *Solid-Phase Extraction*; Elsevier: Amsterdam, The Netherlands, 2020; pp. 37–54. [[CrossRef](#)]
50. Nnadozie, E.C.; Ajibade, P.A. Data for experimental and calculated values of the adsorption of Pb(II) and Cr(VI) on APTES functionalized magnetite biochar using Langmuir, Freundlich and Temkin equations. *Data Brief* **2020**, *32*, 106292. [[CrossRef](#)]
51. Kilic, A.; Karatas, M.E.; Beyazsakal, L.; Okumus, V. Preparation and spectral studies of boronate ester modified magnetite iron nanoparticles (Fe<sub>3</sub>O<sub>4</sub>@APTES-B) as a new type of biological agents. *J. Mol. Liq.* **2022**, *361*, 119602. [[CrossRef](#)]
52. Zhang, Z.; Zhu, Y.; Dai, R.; Zhang, Y.; Wang, H.; Li, J. Enhanced photocytotoxicity induced by a platinum diimine complex employing amine-functionalized magnetite-silica nanocomposites as delivery vehicles. *Photodiagn. Photodyn. Ther.* **2018**, *23*, 50–54. [[CrossRef](#)] [[PubMed](#)]
53. Taufiq, A.; Nikmah, A.; Hidayat, A.; Sunaryono, S.; Mufti, N.; Hidayat, N.; Susanto, H. Synthesis of magnetite/silica nanocomposites from natural sand to create a drug delivery vehicle. *Heliyon* **2020**, *6*, e03784. [[CrossRef](#)] [[PubMed](#)]
54. Ognjanović, M.; Stanković, D.M.; Jaćimović, Ž.K.; Kosović-Perutović, M.; Dojčinović, B.; Antić, B. The effect of surface-modifier of magnetite nanoparticles on electrochemical detection of dopamine and heating efficiency in magnetic hyperthermia. *J. Alloy. Compd.* **2021**, *884*, 161075. [[CrossRef](#)]
55. Kermanian, M.; Sadighian, S.; Naghibi, M.; Khoshkam, M. PVP Surface-protected silica coated iron oxide nanoparticles for MR imaging application. *J. Biomater. Sci. Polym. Ed.* **2021**, *32*, 1356–1369. [[CrossRef](#)]
56. Pomogailo, A.D.; Kydraliev, K.A.; Zaripova, A.A.; Muratov, V.S.; Dzhardimalieva, G.I.; Pomogailo, S.I.; Golubeva, N.D.; Jorobekova, S.J. Magnetoactive Humic-Based Nanocomposites. *Macromol. Symp.* **2011**, *304*, 18–23. [[CrossRef](#)]
57. Stöber, W.; Fink, A.; Bohn, E. Controlled growth of monodisperse silica spheres in the micron size range. *J. Colloid Interface Sci.* **1968**, *26*, 62–69. [[CrossRef](#)]
58. Ozmen, M.; Can, K.; Arslan, G.; Tor, A.; Cengeloglu, Y.; Ersoz, M. Adsorption of Cu(II) from aqueous solution by using modified Fe<sub>3</sub>O<sub>4</sub> magnetic nanoparticles. *Desalination* **2010**, *254*, 162–169. [[CrossRef](#)]
59. Savitzky, A.; Golay, M.J.E. Smoothing and Differentiation of Data by Simplified Least Squares Procedures. *Anal. Chem.* **1964**, *36*, 1627–1639. [[CrossRef](#)]
60. Steinier, J.; Termonia, Y.; Deltour, J. Smoothing and differentiation of data by simplified least square procedure. *Anal. Chem.* **1972**, *44*, 1906–1909. [[CrossRef](#)]
61. Landa, P.; Vankova, R.; Andrlova, J.; Hodek, J.; Marsik, P.; Storchova, H.; White, J.C.; Vanek, T. Nanoparticle-specific changes in *Arabidopsis thaliana* gene expression after exposure to ZnO, TiO<sub>2</sub>, and fullerene soot. *J. Hazard. Mater.* **2012**, *241–242*, 55–62. [[CrossRef](#)]
62. Balzar, D.; Audebrand, N.; Daymond, M.; Fitch, A.; Hewat, A.; Langford, J.I.; Le Bail, A.; Louër, D.; Masson, O.; McCowan, C.N.; et al. Size-strain line-broadening analysis of the ceria round-robin sample. *J. Appl. Crystallogr.* **2004**, *37*, 911–924. [[CrossRef](#)]
63. Toby, B.H. R factors in Rietveld analysis: How good is good enough? *Powder Diffr.* **2006**, *21*, 67–70. [[CrossRef](#)]
64. Bondarenko, L.S.; Pankratov, D.A.; Dzeranov, A.A.; Dzhardimalieva, G.I.; Streltsova, A.N.; Zarrelli, M.; Kydraliev, K.A. A simple method for quantification of nonstoichiometric magnetite nanoparticles using conventional X-ray diffraction technique. *Mendeleev Commun.* **2022**, *32*, 642–644. [[CrossRef](#)]
65. Gorski, C.A.; Scherer, M.M. Determination of nanoparticulate magnetite stoichiometry by Mossbauer spectroscopy, acidic dissolution, and powder X-ray diffraction: A critical review. *Am. Miner.* **2010**, *95*, 1017–1026. [[CrossRef](#)]
66. Frison, R.; Cernuto, G.; Cervellino, A.; Zaharko, O.; Colonna, G.M.; Guagliardi, A.; Masciocchi, N. Magnetite–Maghemite Nanoparticles in the 5–15 nm Range: Correlating the Core–Shell Composition and the Surface Structure to the Magnetic Properties. A Total Scattering Study. *Chem. Mater.* **2013**, *25*, 4820–4827. [[CrossRef](#)]
67. Gallagher, K.J.; Feitknecht, W.; Mannweiler, U. Mechanism of Oxidation of Magnetite to  $\gamma$ -Fe<sub>2</sub>O<sub>3</sub>. *Nature* **1968**, *217*, 1118–1121. [[CrossRef](#)]
68. Bondarenko, L.; Illés, E.; Tombác, E.; Dzhardimalieva, G.; Golubeva, N.; Tushavina, O.; Adachi, Y.; Kydraliev, K. Fabrication, Microstructure and Colloidal Stability of Humic Acids Loaded Fe<sub>3</sub>O<sub>4</sub>/APTES Nanosorbents for Environmental Applications. *Nanomaterials* **2021**, *11*, 1418. [[CrossRef](#)]

69. Li, S.; Wang, J.; Qu, W.; Cheng, J.; Lei, Y.; Liu, M.; Wang, D. Epoxy/Nano-SiO<sub>2</sub> Anticorrosion Coatings Synthesized by Different Molar Ratio of Tetraethyl orthosilicate (TEOS) and Tetramethyl orthosilicate (TMOS). *Int. J. Electrochem. Sci.* **2019**, *14*, 11641–11650. [[CrossRef](#)]
70. Kim, W.; Suh, C.-Y.; Cho, S.-W.; Roh, K.-M.; Kwon, H.; Song, K.; Shon, I.-J. A new method for the identification and quantification of magnetite–maghemite mixture using conventional X-ray diffraction technique. *Talanta* **2012**, *94*, 348–352. [[CrossRef](#)]
71. Pankratov, D.A.; Anuchina, M.M. Nature-inspired synthesis of magnetic non-stoichiometric Fe<sub>3</sub>O<sub>4</sub> nanoparticles by oxidative in situ method in a humic medium. *Mater. Chem. Phys.* **2019**, *231*, 216–224. [[CrossRef](#)]
72. Pankratov, D.A.; Anuchina, M.M.; Spiridonov, F.M.; Krivtsov, G.G. Fe<sub>3</sub>-δO<sub>4</sub> Nanoparticles Synthesized in the Presence of Natural Polyelectrolytes. *Crystallogr. Rep.* **2020**, *65*, 393–397. [[CrossRef](#)]
73. Pankratov, D.A. Mössbauer study of oxo derivatives of iron in the Fe<sub>2</sub>O<sub>3</sub>-Na<sub>2</sub>O<sub>2</sub> system. *Inorg. Mater.* **2013**, *50*, 82–89. [[CrossRef](#)]
74. Oh, S.J.; Cook, D.C.; Townsend, H.E. Characterization of Iron Oxides Commonly Formed as Corrosion Products on Steel. *Hyperfine Interact.* **1998**, *112*, 59–66. [[CrossRef](#)]
75. Klygach, D.S.; Vakhitov, M.G.; Pankratov, D.A.; Zhrebtsov, D.A.; Tolstoguzov, D.S.; Raddaoui, Z.; El Kossi, S.; Dhahri, J.; Vinnik, D.A.; Trukhanov, A.V. MCC: Specific of preparation, correlation of the phase composition and electrodynamic properties. *J. Magn. Magn. Mater.* **2021**, *526*, 167694. [[CrossRef](#)]
76. Chernavskii, P.A.; Kazantsev, R.V.; Pankina, G.V.; Pankratov, D.A.; Maksimov, S.V.; Eliseev, O.L. Unusual Effect of Support Carbonization on the Structure and Performance of Fe/Mgal 2 o 4 Fischer–Tropsch Catalyst. *Energy Technol.* **2020**, *9*, 2000877. [[CrossRef](#)]
77. Jones, D.H.; Srivastava, K.K.P. Many-state relaxation model for the Mössbauer spectra of superparamagnets. *Phys. Rev. B* **1986**, *34*, 7542–7548. [[CrossRef](#)]
78. Nadeem, K.; Krenn, H.; Traussnig, T.; Würschum, R.; Szabó, D.; Letofsky-Papst, I. Effect of dipolar and exchange interactions on magnetic blocking of maghemite nanoparticles. *J. Magn. Magn. Mater.* **2011**, *323*, 1998–2004. [[CrossRef](#)]
79. Adolphi, N.L.; Huber, D.L.; Bryant, H.C.; Monson, T.C.; Fegan, D.L.; Lim, J.; Trujillo, J.E.; Tessier, T.E.; Lovato, D.M.; Butler, K.S.; et al. Characterization of single-core magnetite nanoparticles for magnetic imaging by SQUID relaxometry. *Phys. Med. Biol.* **2010**, *55*, 5985–6003. [[CrossRef](#)] [[PubMed](#)]
80. Klencsár, Z.; Ábrahám, A.; Szabó, L.; Szabó, E.G.; Stichleitner, S.; Kuzmann, E.; Homonnay, Z.; Tolnai, G. The effect of preparation conditions on magnetite nanoparticles obtained via chemical co-precipitation. *Mater. Chem. Phys.* **2018**, *223*, 122–132. [[CrossRef](#)]
81. Kulikova, N.A.; Polyakov, A.Y.; Lebedev, V.; Abroskin, D.P.; Volkov, D.S.; Pankratov, D.; Klein, O.I.; Senik, S.V.; Sorkina, T.; Garshev, A.V.; et al. Key Roles of Size and Crystallinity of Nanosized Iron Hydr(oxides) Stabilized by Humic Substances in Iron Bioavailability to Plants. *J. Agric. Food Chem.* **2017**, *65*, 11157–11169. [[CrossRef](#)]
82. Marcuello, C.; Chambel, L.; Rodrigues, M.S.; Ferreira, L.P.; Cruz, M.M. Magnetotactic Bacteria: Magnetism Beyond Magnetosomes. *IEEE Trans. NanoBiosci.* **2018**, *17*, 555–559. [[CrossRef](#)] [[PubMed](#)]
83. Li, X.; Si, Z.; Lei, Y.; Tang, J.; Wang, S.; Su, S.; Song, S.; Zhao, L.; Zhang, H. Direct hydrothermal synthesis of single-crystalline triangular Fe<sub>3</sub>O<sub>4</sub> nanoprisms. *CrystEngComm* **2010**, *12*, 2060–2063. [[CrossRef](#)]
84. Komogortsev, S.V.; Stolyar, S.V.; Chekanova, L.A.; Yaroslavtsev, R.N.; Bayukov, O.A.; Velikanov, D.A.; Volochaev, M.N.; Eroshenko, P.E.; Iskhakov, R.S. Square plate shaped magnetite nanocrystals. *J. Magn. Magn. Mater.* **2021**, *527*, 167730. [[CrossRef](#)]

**Disclaimer/Publisher’s Note:** The statements, opinions and data contained in all publications are solely those of the individual author(s) and contributor(s) and not of MDPI and/or the editor(s). MDPI and/or the editor(s) disclaim responsibility for any injury to people or property resulting from any ideas, methods, instructions or products referred to in the content.